Nanoscale Advances

ROYAL SOCIETY OF CHEMISTRY

PAPER

View Article Online
View Journal | View Issue

Cite this: *Nanoscale Adv.*, 2023, **5**, 5870

In vitro anti-prostate adenocarcinoma and lung cancer studies of phenoxyaniline-*block*-poly(methyl methacrylate) based nanocomposites *via* controlled radical polymerization

Sahariya Priya, [a] Adhigan Murali, *[b] Sakar Mohan,[c] A. Lakshminarayanan,[d] S. Sekar,[b] R. Ramesh, *[e] M. Devendiran [f] and Sung Soo Han*[a]

Received 14th August 2023
Accepted 14th September 2023

DOI: 10.1039/d3na00644a

rsc.li/nanoscale-advances

A phenoxyaniline-based macroinitiator is utilized for the first time in order to produce phenoxyaniline-*block*-poly(methyl methacrylate) composites through single electron transfer-living radical polymerization (SET-LRP) under mild conditions. A different weight percentage of Cloisite 93A is added into the polymer mixtures in order to increase their biochemical properties. The prepared block copolymer nanocomposites are characterized using ATR-IR, UV-vis-spectroscopy, XRD, Raman, TGA, DSC, a particle size analyzer, contact angle measurements and SEM in order to characterize their structural, thermal, surface and morphological properties. Further, the developed polymeric nanocomposites are successfully applied in two different cancer cell lines (prostate adenocarcinoma and lung cancer), which show excellent anticancer properties. Also, acridine orange/ethidium bromide (AO/EtBr) dual staining is performed, which causes drastic cell death by apoptosis in both A549 and PC-3 cell lines, which indicated that the prepared polymeric nanocomposites effectively inhibit the cell proliferation and induce the apoptosis in both the cancer cells. Here nanoclay is used for cancer treatment because of its complete water solubility, which essentially causes the formation of a cationic complex between the clay and drug through electrostatic interactions. Hence, the exchange of ions between the clay and other ions in the biological environment leads to inhibition of the proliferation of prostate adenocarcinoma and lung cancer cells in the system.

1 Introduction

To date, chemotherapy is one of the major techniques to treat many cancers. However, during the chemotherapy treatment, some healthy cells can also be destroyed, leading to serious side effects. In order to address this issue in the chemotherapy treatments of various tumour cells, some alternative cancer treatments have emerged, including targeted drug delivery systems.[1] Nano-based drugs or medicines are playing a major role in this field by contributing many advantages over drug delivery methods, diagnosis, enhanced cancer imaging, targeting of particular cancer cells, *etc.* Moreover, nano-based drugs can enhance active or passive cancer targeting and thus increase the selectivity, lower the toxicity and prolong the half-life span in the human body. Also, surface-charge of nanoparticles (such as clay particles) plays an important role in their interaction with the cell surface for effective cellular uptake.[2] Modifying an existing drug is an important approach for the progress of novel anti-cancer agents.

In this direction, Kumar *et al.* reported azo-Schiff base ligands like 2-((*E*)-((4-(diethylamino)phenyl)imino)methyl)-4-((*E*)-((2-phenylamino)phenyl)diazinyl)phenol containing Zn(II) complexes, which have been analyzed for their effective cytotoxicity properties against the Hut-78 cell line.[3] Hosseini *et al.* also reported a doxorubicin-based bentonite nanoclay complex and used it to treat melanoma cells, which showed effective targeted drug delivery properties.[4] Generally, nanoparticulate clay, which we used in anti-cancer treatment, has drawn great attention as a drug carrier due to their better bio-compatibility, high specific surface area and high adsorption behavior. For example, aluminosilicate-based nanoclay acts as an excellent

[a]*School of Chemical Engineering, Yeungnam University, 280 Daehak-Ro, Gyeongsan, Gyeongbuk 38541, Republic of Korea. E-mail: sshan@yu.ac.kr*

[b]*School for Advanced Research in Petrochemicals (SARP)- ARSTPS, Central Institute of Petrochemicals Engineering & Technology (CIPET), Govt. of India, Chennai, 600032, India. E-mail: precymurali@gmail.com*

[c]*Centre for Nano and Material Sciences, Jain University, Bangalore 562112, Karnataka, India*

[d]*Department of Pharmacology, Indira Medical College and Hospitals, Tiruvallur, Tamilnadu, 631 203, India*

[e]*Department of Chemical Engineering, School of Mechanical, Chemical and Material Engineering, Adama Science and Technology University, Adama, P.O. Box: 1888, Adama, Ethiopia. E-mail: ramesh.redrouthu@astu.edu.et*

[f]*Vels Institute of Science Technology and Advanced Studies (VISTAS), Pallavaram, Chennai 117, India*

drug delivery carrier in cancer cell lines for particular tumour sites.[5] On the other hand, the most frequently used acrylic derivative polymers such as polymethyl methacrylate, polymethacrylic acid and acrylamide enable the effective controlled-release of drugs in active tumour cells.[6,7] Rao *et al.* reported acrylic derivative-based PMMA microgels for the controlled release of an anti-cancer treatment, which suggested that the ionic transport was controlled more by relaxation of poly(-methacrylic acid) gel due to the occurrence of ionization of carboxylic groups through electrostatic repulsion between adjacent ionized groups.[8,10] Seyedeh *et al.*[10] also reported PMMA coated chitosan–glutathione conjugates, which have been analyzed for their anticancer activities against NIH 3T3 and T47D breast carcinoma cells, and HT29 and CaO_2 colon cell lines. Several researchers have attempted to synthesize various co-polymer materials (di-block or triblock) for anticancer treatments thanks to their sensitivity, selectivity, compatibility and low cytotoxicity with different cancer cell lines. In this way, Caner *et al.* reported a paclitaxel-based drug loaded amphiphilic star hyperbranched block copolymer for targeted anti-cancer applications.[9] In this direction, herein, we have utilized the above characteristic behavior of copolymers in cancer cells and to the best of our knowledge, this is the first time that phenoxyaniline-*block*-PMMA through single electron transfer-living radical polymerization has been introduced for anticancer treatments against prostate adenocarcinoma and lung cancer cell lines.

2 Experimental

2.1 Materials

Methyl methacrylate (MMA: $C_5H_8O_2$, M_w: 100.12 g mol^{-1}, and 99% purity) monomer and 3-phenoxyaniline ($C_{12}H_{11}NO$, M_w: 185.22 g mol^{-1}, and 98% purity) were procured from Sigma-Aldrich, USA and the monomer was further purified by passing it through an alumina column (removal of inhibitor) before use. Bromoisobutyryl bromide [$(CH_3)_2CBrCOBr$], *N*,*N*,N^{I},N^{II},N^{III}-pentamethyldiethylenetriamine [PMDETA, $[(CH_3)_2NCH_2CH_2]_2NCH_3$)], and copper (0) powder, 99.9% were received from Sigma-Aldrich, USA and used as received. Cloisite 93A (particle size <2 μm) was obtained from Rockwood Additives. Organic solvents (dimethyl sulfoxide (DMSO), triethylamine (Et_3N), dimethyl formamide (DMF), tetrahydrofuran (THF), and hexane were dried and distilled before use. Lung cancer cell lines (A549) and human prostate cancer cell lines (PC-3) were purchased from the National Centre for Cell Science (NCCS), Pune, India. Cell Proliferation Kit I (MTT), acridine orange (AO), ethidium bromide (EtBr) and phosphate buffered saline (PBS) were procured from Sigma-Aldrich, USA.

2.2 Characterization methods

Raman spectra were recorded on a confocal Raman spectrometer (Alpha 300R, WITec GmbH, Germany, excited at 532 nm using a Ne laser). FT-IR spectra of polymeric materials were analyzed using a Thermo Scientific-NICOLET 6700 model in transmittance mode. Scanning electron microscopy (SEM) was performed using a JEOL JSM-IT800 with a super hybrid lens operated at 30 kV to afford the images. The particle size distribution analyses were performed on a Litesizer 500 model from Anton Paar, USA. Thermal analysis was executed using a DSC Q-200 and TGA Q-50 from TA Instruments (WATERS), Austria. Molecular weight distribution was determined by gel permeation chromatography (GPC) (instrument from Shimadzu, Japan). UV-vis absorption spectra were recorded on an Elico SL-159 spectrometer and X-ray diffraction (XRD) was performed using Cu Kα = 1.54060 Å (instrument from Rigaku, Japan). The surface wettability of the coated film was measured using the water contact angle (Halmarc HO-IAD-Cam-O1B). A micro-ELISA plate reader and flow cytometer were used and cells were washed two times before analysis of fluorescence intensity, further stained and viewed under a fluorescence microscope at 20× magnification.

2.3 Cell viability (MTT) assay

The cell viability of DST-28 (phenoxyaniline-*b*-PMMA with nanoclay) treated PC-3 cells was assessed by MTT assay. The assay is based on the reduction of a soluble yellow tetrazolium salt to insoluble purple formazan crystals by metabolically active cells. PC-3 cells were plated in 48 well plates at a concentration of 2×10^4 cells per well. 24 hours after plating, cells were washed twice with 500 μL of serum-free medium and starved by incubating the cells in the serum-free medium for 3 hours at 37 °C. After starvation, cells were treated with DST-28 at different concentrations (10–120 μg mL^{-1}) for 24 hours. At the end of treatment, the medium from the control and DST-28 treated cells was discarded and 200 μL of MTT containing DMEM (0.5 mg mL^{-1}) was added to each well. The cells were then incubated for 4 h at 37 °C in a CO_2 incubator. The MTT containing medium was then discarded and the cells were washed with 1× PBS. The crystals were then dissolved by adding 200 μL of solubilization solution and this was mixed properly by pipetting up and down. Then the formazan crystals formed were dissolved in dimethyl sulfoxide (200 μL) and incubated in the dark for an hour. Then the intensity of the color developed was assayed using a micro-ELISA plate reader at 570 nm. The number of viable cells was expressed as a percentage of control cells cultured in a serum-free medium. Cell viability in the control medium without any treatment was represented as 100%. The cell viability is calculated using the formula: % cell viability = [570 nm treated cells/570 nm control cells] × 100. Based on the MTT assay, we selected the optimal doses (IC-50: 40 μg mL^{-1}) for further studies. Analysis of cell morphology changes using a phase-contrast microscope: 3×10^4 cells were seeded in 6 well plates and treated with DST-28 (40 μg mL^{-1} for PC-3 cells) for 24 h. At the end of the incubation period, the medium was removed and cells were washed once with phosphate buffered saline (PBS pH 7.4). The plates were observed under a phase-contrast microscope. Cell viability of DST-24 treated A-549 lung cancer cell lines was assessed using MTT assay. The assay was based on reducing the soluble yellow tetrazolium salt to insoluble purple formazan crystals by metabolically active cells. In this study, the A-549 cells were

plated in 48 well plates (2×10^4 cells per well). After 24 h, cells were washed twice with 500 μL serum free medium and starved for 3 h at 37 °C. Then, the cells were treated with DST-24 (25–150 μg mL^{-1}) for 24 h. After treatment, control and treated cell media were discarded. The MTT (200 μL, 0.5 mg mL^{-1} in DMEM) was added, incubated for 4 h at 37 °C, and then discarded. Cells were washed with 1× PBS. The crystals were dissolved using 200 μL solubilization solution, mixed and then dissolved in DMSO (200 μL). Intensity was measured at 570 nm using a micro-ELISA plate reader. Viable cells were expressed as a percentage of control in serum-free medium (100%) for untreated control. Optimal doses (IC-50: 50 μg mL^{-1}) were selected based on MTT assay. The change in cell morphology was analyzed using a phase-contrast microscope. Around 3×10^4 cells seeded in 6-well plates were treated with DST-24 (50 μg mL^{-1}) for A-549 cells for 24 h. After incubation, the medium was removed, and cells were washed with PBS (pH 7.4).

2.4 Determination of the mode of cell death by acridine orange (AO)/ethidium bromide (EtBr) dual staining

The effects of DST-28 in PC-3 cell death were also determined by AO/EtBr dual staining as described previously.[11] The cells were treated with DST-28 for 24 h and then the cells were harvested and washed with ice-cold PBS. The pellets were resuspended in 5 μL of acridine orange (1 mg mL^{-1}) and 5 μL of EtBr (1 mg mL^{-1}). The apoptotic changes of the stained cells were then observed using a fluorescence microscope.

2.5 Synthesis of the phenoxyaniline (PA) based macroinitiator

0.37 g of 3-phenoxyaniline was dissolved in 15 mL of DCM, further transferred into a 50 mL round-bottom flask and kept in an ice bath. After 30 min, 0.54 mL (2 mM) of trimethylamine was added to the above mixture and stirred for another 30 min at 0 °C. Ice cubes were added into the ice bath to bring the temperature to 0 °C. After, that 0.48 mL (2 mM) of α-bromoisobutrylbromide was added drop by drop using a glass syringe and stirred for 24 h at 0 °C under a N_2 atmosphere (see Scheme 1). Finally, 20 mL of diethylether was used to terminate the reaction and further obtain white color crystals (PA-initiator).

2.6 Preparation of phenoxyaniline-*b*-PMMA through the SET-LRP method

0.25 g of 3-phenoxyaniline-based initiator was dissolved in 5 mL of tetrahydrofuran (THF) and 2 mg of degassed Cu(0) powder was added into the above mixture. The mixture was transferred into a 50 mL round bottom flask. Further, deoxygenated MMA (4.0 mL) was added to the mixture *via* syringe and the reaction mixture was degassed by four freeze–pump–thaw cycles. Finally, 4.63 mg of PMDETA was added to the mixture and stirred in a thermostatic oil bath at 65 °C for 20 h under a N_2 atmosphere. After that, different concentrations of Cloisite 93A [DST-24 (0%), DST-25 (1%), DST-27 (2%), and DST-28 (3%)] were dissolved in 3 mL of THF and added into the above mixture and further stirred at 60 °C for 4 h. After 24 h, the polymer functionalization reaction was terminated by pouring the mixture into 150 mL of hexane. The resulting precipitate was filtered, redispersed in 100 mL of THF and again precipitated to remove the unreacted monomer and Cu(II)/PMDETA complex. The procedures were repeated several times before analyzing the molecular weight by GPC. A pale gray solid was obtained after vacuum drying for 30 h (see Scheme 2). All the experimental data are depicted as the mean of two or three individual experiments. Deviations from mean differences are presented as mean ± SD. The cells were treated with different concentrations (0, 25, 50, 75, 100, 125 and 150 μg) for 24 h.

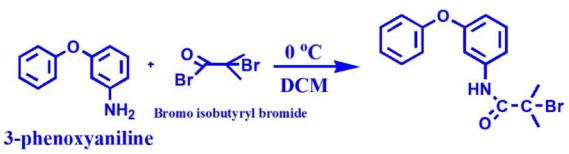

Scheme 1 Synthesis of the phenoxyaniline based macroinitiator.

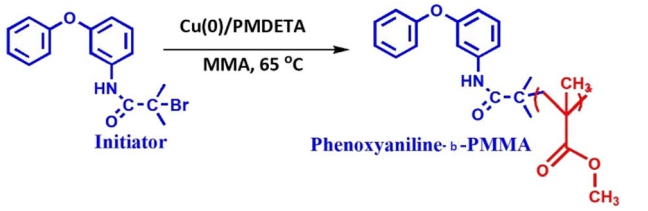

Scheme 2 Synthesis of phenoxyaniline-*b*-PMMA through SET-LRP.

2.7 Statistical analysis

The cytotoxic effects of DST-24 on A549 cells were determined using the MTT assay. The cells were treated with different concentrations (0, 25, 50, 75, 100, 125 and 150 μg) for 24 h. 50% inhibition was observed at a concentration of 50 μg mL^{-1} (p value: 0.0215), which was taken as the IC-50 value for further experiments. Data are presented as mean ± SD ($n = 3$). *Significant compared with the control-blank group, $p < 0.001$.

For the cytotoxic effect of DST-28 on the prostate cancer cell line, cells were treated with different concentrations (10, 20, 40, 80, 100, and 120 μg mL^{-1}) for 24 h. 50% inhibition was observed at a 40 μg mL^{-1} (p-value: 0.0037) concentration, which was taken as the inhibitory concentration (IC-50) dose value and fixed for further experiments. * signifies statistical significance between control and treatment groups at the $p < 0.05$ level using the Student–Newman–Keuls test.

3 Results and discussion

3.1 Structural identification by FT-IR and XRD

The FTIR spectra for phenoxyaniline initiator (PA), DST-24, DST-25, DST-27 and DST-28 samples were recorded in the range of 4000–500 cm^{-1} as shown in Fig. 1a. In the initiator spectrum, the stretching band at 3334 cm^{-1} assigned to the N–H stretching vibration is indicative of the existence of an amine group in

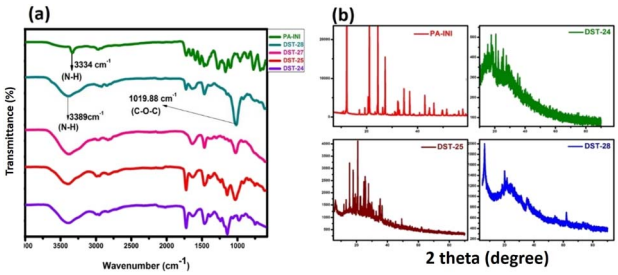

Fig. 1 FT-IR spectra of (a) the phenoxyaniline initiator (PA-INI) and different weight percentages of polymer nanocomposites *via* SET-LRP [DST-24: phenoxyaniline-*b*-PMMA, without clay, DST-25: 1% clay containing phenoxyaniline-*b*-PMMA, DST-27: 2% clay containing phenoxyaniline-*b*-PMMA, DST-28: 3% clay containing phenoxyaniline-*b*-PMMA] and (b) XRD pattern of the phenoxyaniline initiator and its composites [DST-24, DST-25 and DST-28].

the initiator. The presence of an aromatic amine group is also confirmed by a peak at 1272 cm^{-1} (C–N stretching). Further, the cyclic alkene is confirmed by the peak at 1657 cm^{-1} (C=C stretching); the notable peak at 687 cm^{-1} is attributed to the C–Br stretching vibration and it indicates the presence of a halide anion in the initiator, which confirms the existence of phenoxyaniline in the PA sample. DST-24, DST-25, DST-27 and DST-28 composite samples have predominant peaks at 3389 cm^{-1}, which indicates the existence of N–H stretching vibration. The band at 1726 cm^{-1} is the C=O (stretching) vibration band of PMMA and the peaks between 740 and 1300 cm^{-1} have become broad owing to the C–O–C band stretching mode of the ester moiety from PMMA.[12]

Compared to the PA initiator, the N–H stretching vibration band is shifted from 3334 to 3389 cm^{-1} in all DST-24, DST-25, DST-27 and DST-28. The vibrational peaks at 1386 cm^{-1} and 748 cm^{-1} could be attributed to the α-methyl group vibrations and the peak at 1468 cm^{-1} can be assigned to the C–H bending vibration of the $-CH_3$ group in PMMA.[13] The peak at 1636 cm^{-1} is assigned to the C=C (stretching cyclic alkene) band of PMMA. Overall, the synthesized polymer units and initiator functional groups are confirmed by the FT-IR technique. Further, XRD analysis was carried out to investigate the crystalline and phase formation of the synthesized materials. Fig. 1b shows the X-ray diffraction peaks at 21.81°and 63.87° (JCPDS No.: 04-0783) corresponding to the diffraction planes of (100) and (220), respectively, which is attributed to the existence of phenoxyaniline in the PMMA composite. Fig. 1b shows the X-ray pattern of the phenoxyaniline-based initiator, which shows peaks at 2θ = 18.71°, 20.61°, 20.91°, 25.93°, 29.96°, 31.02°, 31.43°, 32.27° and 41.689°, which correspond to the diffraction planes of (100), (100), (100), (100), (110), (110), (110), (110), and (200) respectively. The narrow peaks of the XRD patterns clearly confirm their improved crystalline properties. The narrow peak at 20.61° corresponds to the highly crystalline nature of the system, which can be attributed to the presence of halide groups, which is also confirmed by SEM images as shown in Fig. 4. Interestingly, while preparing the PA sample, many white colour crystals were formed in the Petri dish as shown in Fig. 4c. Notably, after polymerization, the composite becomes amorphous in nature for all the samples (DST-24, DST-25 and DST-28) due to incorporation of Cloisite at different weight percentages. This can be due to the destruction of the ordered arrangements of the methacrylate in the composite. This emerged amorphous phase can cause a reduction in the energy barrier of polymer chain segmental motion. Further, the obtained XRD pattern clearly shows that the crystallinity of the blends is decreased after it is blended with PMMA and it becomes more amorphous in nature, which eventually causes a greater ionic diffusion and ionic conductivity, and hence it becomes viable to inhibit the cancer cells.

3.2 Raman spectroscopy study

Details of the intra- and inter-molecular mechanism of interaction between phenoxyaniline and PMMA were investigated by Raman spectroscopy using a 532 nm laser in the spectral region 50–3500 cm^{-1}.

The methylene group (CH_2 at 838 cm^{-1}) which is present in the PMMA and the CH_3 groups at 980 cm^{-1} that are attached to the backbone of carbon and the single oxygen atoms are denoted as α-methyl and the ester methyl and the carbonyl (C–O at 1743 cm^{-1}) groups are found to be attached to the carbon backbone respectively.[14] However, some of the Raman modes are found to be very weak in their respective region. For example, the C–C–O symmetric stretching mode at 608 cm^{-1}, carbonyl group at 1743 cm^{-1} and C–O–CH_3 at 810 cm^{-1} in all three composite samples are given in Fig. 2(b–d). Notably, the Raman shift is increased with increasing nanoclay content in the PMMA matrixes. Fig. 2a shows the spectrum of the phenoxyaniline based initiator. The spectrum clearly reveals the functional group at 1010 cm^{-1} (C–O–C) and sharp N–H peak at 3313 cm^{-1}, which confirmed the formation of the phenoxyaniline structure. The specially prepared composition with the highest percentage of clay, containing phenoxy-*b*-PMMA with

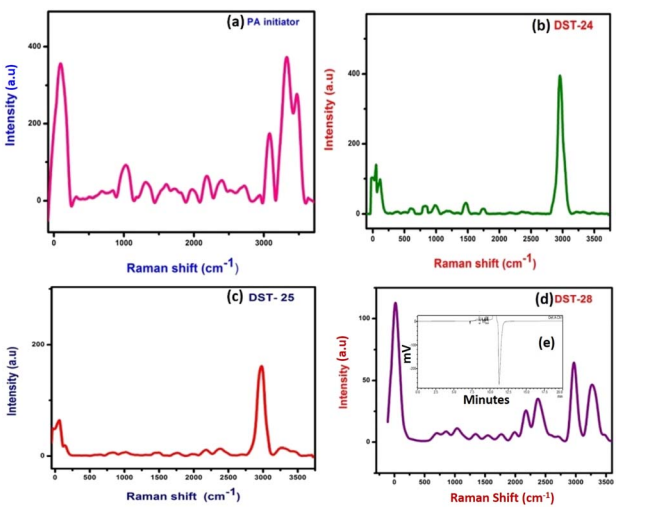

Fig. 2 Raman spectra of (a) phenoxyaniline initiator, (b) DST-24 (phenoxyaniline-*b*-PMMA, without clay), (c) DST-25 (1% clay containing phenoxyaniline-*b*-PMMA) and (d) DST-28 (3% clay containing phenoxyaniline-*b*-PMMA), and (e) GPC of DST-28 (3% clay containing phenoxyaniline-*b*-PMMA).

M_n: 3112, M_w: 3595 and PDI: 1.15 as shown in Fig. 2e, confirms the success of controlled radical polymerization.

3.3 UV-vis spectroscopy, particle measurements and thermal study

The DSC experiment was carried out in the temperature range from −50 °C to 250 °C with a heating rate of 10 °C min^{-1} under a nitrogen atmosphere. The polymer composite sample of 12 mg was encapsulated in an aluminum pan. The DSC plot of the polymer containing 3% filler shows the sharp exothermic peak, which indicates the transition from a semi-crystalline to amorphous phase. DSC results showed that the T_g of phenoxyaniline-*b*-PMMA (DST-28) is ∼115 °C (see Fig. 3a). The decrease in T_g could be due to the addition of Cloisite 93A, which increases the segmental motion of the polymer unit.

The pure PMMA has a melting temperature of around 160 °C, but phenoxyaniline-*block*-PMMA has a decreased T_g. The softening temperature is found to decrease when the symmetrical structure is changed into an asymmetrical structure, which implies that there is a reduction in the crystallinity of the polymer composite. There are three main stages of degradation of phenoxyaniline-*b*-PMMA. Moreover, the first stage is complex for all the samples except pure PMMA. The polymer content in the phenoxyaniline is determined by means of TGA, which confirms the growth of the polymer on the surface through various weight loss measurements. The TGA trace for phenoxyaniline-*b*-PMMA shows a significant shift in the weight loss towards higher temperature with a thermal stabilization of 30 °C, which is higher than that for a neat PMMA. The enhanced thermal stability observed for phenoxyaniline-*b*-PMMA composites is influenced by the interaction between the polymer and Cloisite, as evident from the thermogram (Fig. 3b). The TGA curve of the initiator distinguishes two weight loss stages during the thermal decomposition of the sample. The first stage shows the decomposition or loss of the absorbed and combined water and the evaporation of residual solvent. In the second stage, after 330 to 450 °C, it shows some decomposition of the sample. While increasing the filler content in the polymer network, the thermal stability is also increased. The DST-28 sample with 3% Cloisite 93A shows a drastic weight loss, which may be attributed to the melting of the polymer. The prepared polymer composites are stable up to 450 °C. For the contact angle measurements by the sessile drop method, a Holmarc HOIIDCAM-01B contact angle meter (India) video-camera system equipped with computer software was used. The contact angles of probe liquid were measured at 20 ± 1° in a closed chamber. The advancing contact angle of water of 100 μL volume was measured after settling droplets on the glass surface. Then after sucking one-third of the droplet into the syringe, the receding contact angle was measured. Fig. 3d shows a good hydrophilic nature (DST-24, CA: 63°); however, upon increasing the concentration of Cloisite 93A in the polymer mixture (DST-25, CA: 80° and DST-28, CA: 121°), it becomes hydrophobic in nature, which means that the polymer composite has better wettability. Moreover, we also analyzed the particle size of the polymer composite using a particle size analyser, which show the average particle size is around 953 nm (see Fig. 3c). The UV visible spectra of the initiator and DST-28 have been analyzed ranging from 300 to 600 nm. In Fig. 3e the maximum absorption was obtained at 300 nm, which is due to the saturated aliphatic polymer with a carbonyl group as a chromophore. The most typical absorption band for carbonyl compounds is that of the n–π* transition. This transition usually requires the smallest energy so that the band has the largest wavelength in the region of 280–300 nm. Interestingly, there is no evidence of absorption in the range of 400 to 800 nm for both the samples. In Fig. 3e, the initiator was used to polymerize the MMA monomer where the band is observed at 300 nm and it is found that it is slightly broad up to 450 nm due to the well-controlled polymerization. This n–π* transition is "forbidden" in symmetry terms and, therefore, the intensity is low after polymerization. The observed low intensity absorption band at 320 nm may be due to the n–σ* transition occurring in carbonyl groups present in PMMA molecules.

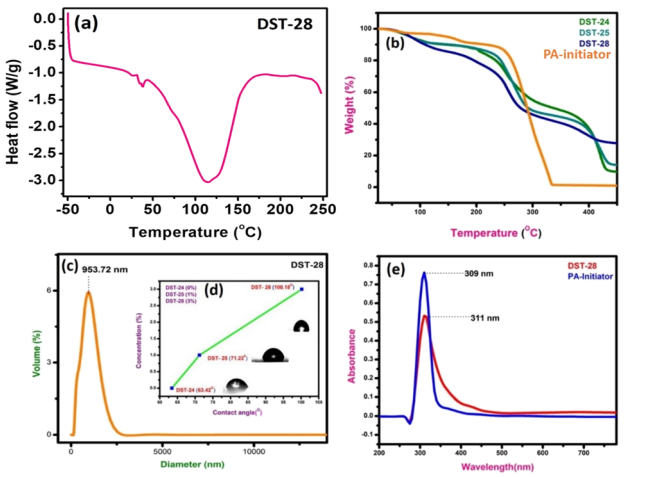

Fig. 3 (a) Differential scanning calorimetry (DSC) thermogram of DST-28 (enthalpy: 599.51 J g^{-1}, 10 °C min^{-1}), (b) thermogravimetric analysis (TGA) of various percentages of polymer composites: DST-24 (phenoxyaniline-*b*-PMMA, without clay), DST-25 (1% clay containing phenoxyaniline-*b*-PMMA), DST-28 (3% clay containing phenoxyaniline-*b*-PMMA) and phenoxyaniline initiator, (c) particle size analysis of DST-28 (3% clay containing phenoxyaniline-*b*-PMMA), (d) contact angle measurements of different percentages of composites: DST-24 (phenoxyaniline-*b*-PMMA, without clay), DST-25 (1% clay containing phenoxyaniline-*b*-PMMA), DST-28 (3% clay containing phenoxyaniline-*b*-PMMA) and (e) UV-vis spectra of the macroinitiator with the highest percentage of the composite (DST-28 with 3% clay).

3.4 Morphological study by SEM

Phenoxyaniline was brominated using bromoisobutryl bromide in dichlromethane solvent medium; after reaction, the mixture was washed with diethyl ether several times and kept at room temperature. After 2 days, we observed that white colour crystals were formed after complete evaporation of the organic solvent, which is shown in Fig. 4c. The same sample was analyzed by

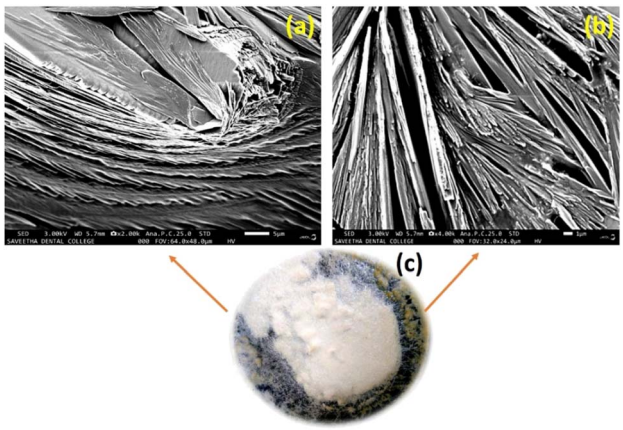

Fig. 4 Scanning electron microscopy (SEM) images of the phenoxyaniline initiator after complete removal of organic solvent with layer by layer white crystals: (a) 5 μm size, (b) 1 μm size and (c) photographic image of the white crystal based phenoxyaniline initiator.

SEM, which showed layer by layer crystals with an average width of ~100 nm (see Fig. 4a and b). It has already been recommended that the morphology of layered crystals of the PA macroinitiator strongly depended on the agreeing solvent evaporation rate. A low solvent evaporation typically leads to higher formation of crystals.

The prepared initiator and polymer composite samples were investigated through SEM to evaluate the surface changes with and without the filler. Further, the macroinitiator was utilized to polymerize the MMA monomer to afford porous polymer composites. In Fig. 5a, the SEM micrograph of DST-24 clearly shows the porous like structure. A quite homogeneous pore distribution was obtained without the filler (Cloisite) with an average pore size of 97 nm (see Fig. 5a–e). Subsequently, in the micrograph of DST-28 containing 3% Cloisite 93A, it is observed that there are less macropores due to the higher percentage of clay content in the PMMA network and some of the cell windows are closed in the pore walls. The polymer composites were also subjected to XRD, which clearly agreed with the formation of amorphous and crystalline phases. SEM images also clearly suggested that the incorporation of clay content in the polymer matrixes led to an intercalated well and the higher percentages of clay led to the agglomerated structure as shown in Fig. 5f–j and all the clay layers were found to have an average size of 159–163 nm, and thus could not be homogeneously dispersed in the PMMA matrix.[15]

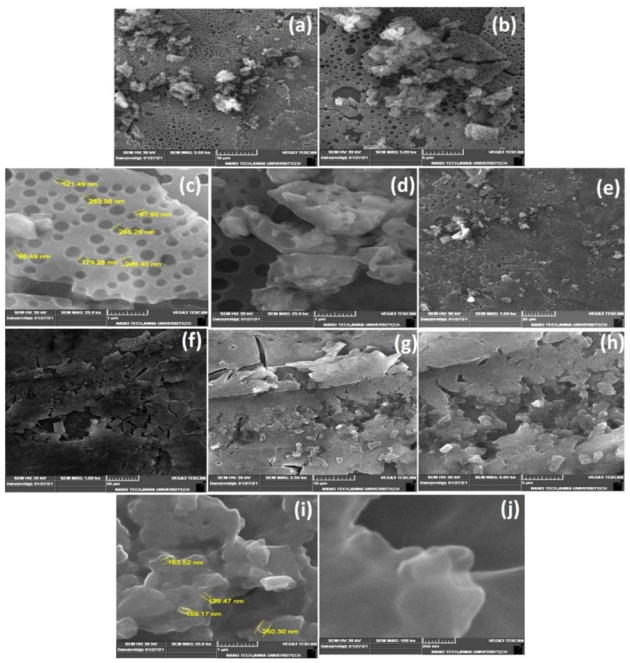

Fig. 5 SEM images of phenoxyaniline-*b*-PMMA without clay content from (a) to (e): (a) porous structure at 10 μm, (b) 5 μm size, (c and d) 1 μm with an average pore size diameter of 172 nm and (e) 20 μm size. (f–j) Phenoxyaniline-*b*-PMMA with 3% clay content: (f) 20 μm size, (g) 10 μm size, (h) 5 μm size, (i) 1 μm with clay flakes approximately 170 nm in diameter, and (j) 200 nm size.

3.5 Anticancer activities of phenoxyaniline-*b*-PMMA (without nanoclay) against lung cancer (A549)

Based on the MTT assay, it can be inferred that there was a significant cytotoxic activity of DST-24 against lung cancer cell lines (A549). It was identified that the inhibitory concentration for this DST-24 is 50 μg mL^{-1}.

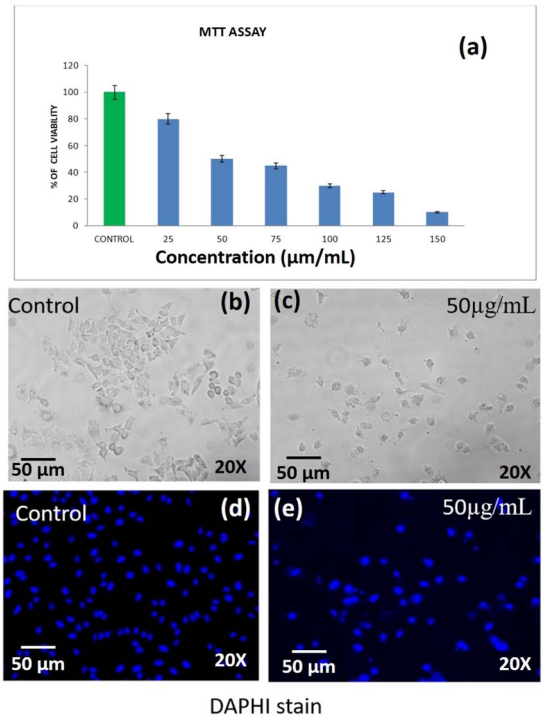

Fig. 6 (a) MTT assay of DST-24 on A549 cells, (b and c) morphological changes in the lung cancer cell line without and with treatment of DST-24 at 50 μg mL^{-1} for 24 h using a phase contrast microscope at 20× magnification (scale bar 50 μm), (d and e) induction of apoptosis in the DST-24 treated lung cancer cell line and nuclei were stained with DAPI staining and observed under a fluorescence microscope (20× magnification, scale bar 50 μm).

Table 1 Percentages of cell viability against A-549 cell lines

S. No.	IC-50, cell viability test against lung cancer cell lines (A-549)-DST-24							
1	Concentration	Control	25	50	75	100	125	150
	Percentage of cell viability	100	80	50	45	30	25	10

Comparison of the cell morphology showed the differences in the cell morphology of the control and the cell morphology of the cell lines treated with the DST-24. It was observed that the number of cells decreased after treatment and the cells exhibited cell shrinkage and cytoplasmic membrane blebbing (see Fig. 6). Previous studies also analyzed the changes in cellular morphology of the cancer cell line. Their studies also confirmed similar cellular changes with increased free-floating cells.[16,17] The DAPI staining apoptosis test results suggest that there was condensation of chromatin and nuclear fragmentation which occurred owing to the process of apoptosis.[18] These changes were observed under fluorescence microscopy. These results obtained in our study are supported by the similar studies done previously, where the most anti-cancer effects are based on the apoptotic activity of the chemotherapeutic agents.[19,20] However, future *in vivo* studies need to be performed for better understanding and usage of phenoxyaniline-*b*-PMMA as a cytotoxic agent. Also, IC-50 doses and cell viability against A-549 cell lines are shown in Table 1.

3.6 Anticancer activities of DST-28 against the prostate adenocarcinoma cancer cell line (PC-3)

Apoptosis is a programmed cell death that serves as an important mechanism for tissue homeostasis and cell eradication and by inhibiting metabolic activation, boosting detoxification, or offering alternate targets for electrophonic metabolites, these substances aid in the prevention of carcinogenesis.[22,23] The cytotoxic effect of DST-28 extract on cell lines was calculated by micro-culture tetrazolium assay (MTT). The multiple concentration of DST-28 was used and IC50 doses were calculated (see Table 2). The MTT assay results showed that the dose dependent (10–120 μg mL^{-1}) cell growth inhibition was observed in DST-28 treated against PC-3 cells. The IC-50 dose was observed at 40 μg mL^{-1}. Since DST-28 has better cytotoxic activity against PC-3 cells, it was used for further investigation. Morphological investigation of apoptosis revealed that DST-28 at a concentration of 40 μg mL^{-1} induced cell death in the PC-3 cell line by apoptosis. Phenotypically, apoptosis is characterized by cell shrinkage, DNA fragmentation, chromatin condensation, plasma membrane blebbing, and collapse of the cell into small membranes. The phase-contrast image shows that DST-28 exhibits morphological changes such as reduction in the number of cells, cell shrinkage, and cytoplasmic membrane blebbing in the treated cells when compared with untreated cells. The DST-28 exhibited exceptional antioxidant activity in all antioxidant tests and significantly reduced lipid peroxidation at a concentration of 50 g mL^{-1}, according to a prior research report.[21,24] AO/EtBr (acridine orange and ethidium bromide) dual staining was performed to determine if exposure to DST-28 causes cell death by apoptosis in PC-3 cell lines. In the AO/EtBr staining, the viable cells will possess a uniform bright green nucleus. The early apoptotic cell will have bright orange areas of condensed or fragmented chromatin in the nucleus. Late apoptotic cells will have a uniform bright red nucleus. It was found that untreated cells were mostly green with an intact nucleus. AO/EtBr analysis showed that DST-28 was cytotoxic to PC-3 cells through apoptosis when treated with IC50 concentration (40 μg mL^{-1}). In the AO/EtBr analysis, cells treated with IC-50 value of DST-28 showed a red color nucleus, which further confirmed the induction of late apoptosis in PC-3 cells by DST-28 (see Fig. 7). This finding was characterized by membrane blebbing and nuclear shrinkage.

Table 2 Percentages of cell viability against PC-3 cell lines

S. No.	IC-50, cell viability test against prostate cancer cell lines (PC-3)-DST-28							
1	Concentration	Control	10	20	40	80	100	120
	Percentage of cell viability	100	80	50	45	30	25	10

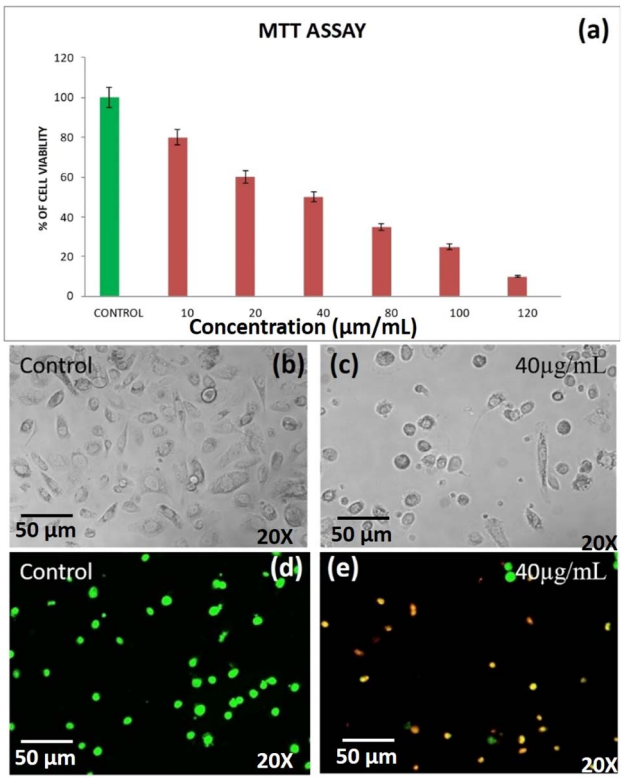

Fig. 7 (a) Cytotoxic effect of DST-28 (with nanoclay) against the prostate cancer cell line, (b and c) phase-contrast microscopy images of the DST-28 compound on cell morphological changes in the prostate cancer cell line (20× magnification, 50 μm scale bar), (d and e) the PC-3 cells treated with DST-28 at 40 μg mL^{-1} concentration and viewed under a fluorescence microscope at 20× magnification (scale bar 50 μm).

The above data indicate that DST-28 inhibits cell proliferation and induces apoptosis in prostate cancer cells.

Conservative precision medicine for cancer treatment is one of the most promising methods to undertake various cancers by developing the effective drugs. In this study, we developed a novel polymer nanocomposite as an anti-cancer drug molecule to treat lung and prostate cancers. Phase contrast microscopy was used to analyse the changes in cell morphology of the lung cancer cell lines when treated with DST-24 (without nanoclay). The changes in cell morphology among the lung cancer cell lines treated with 50 μg mL^{-1} concentration DST-24 was compared with the control group for 24 hours. The results suggest that the treated cells showed characteristic changes similar to that of apoptotic cells – shrinkage of cells with reduced cell density. Some cells also showed other changes much like that of apoptotic cells like cell roundening and loss of contact with adjacent cells. Some cells detached themselves from the base of the plates. DAPI staining was used to analyse the induction of apoptosis among the lung cancer cell lines treated with DST-24 (50 μg mL^{-1}) after 24 hours. Fluorescence microscopy was used to check the pro-apoptotic effect post staining. The results suggested that the cancer cell lines treated with the leaf extract showed condensation of chromatin along with nuclear fragmentation. These changes are suggestive of characteristic apoptotic activity when compared to the control group which had round nuclei. MTT assay was used to assess the cytotoxic potential of phenoxyaniline-*b*-PMMA (DST-24) on the lung cancer cell lines. Various concentrations of the extract (25–150 μg mL^{-1}) were tested against the lung cancer cell line for 24 hours. The results of the assay suggested that there was a significant decrease in the viability of lung cancer cell lines (A-549) when treated with DST-24, when compared to the control for 24 hours. The viability of the cells was gradually decreased with increasing concentration of the DST-24. It was observed that 50% growth inhibition occurred at a concentration of 50 μg mL^{-1}. Thus, the IC-50 dose considered for further experiments was about 50 μg mL^{-1} (see Fig. 6a). Further, we studied the anti-cancer activity of DST-28 against the prostate adenocarcinoma cancer cell line (PC-3). It showed prominent results in the prostate cancer cell line. DST-28 has an excellent cytotoxic effect against PC-3 cell lines; further, its effect was investigated on their cell morphological behaviors under fluorescence and contrast microscopy and it caused cell shrinkage, DNA fragmentation, chromatin condensation, plasma membrane blebbing, and collapse of the cell into small membranes. Cloisite 93A nanoclay, with its specific chemical composition, surface-area-to-volume ratio, charge and size, possesses good surface properties that can interfere with the function of cancer cells, disrupting cellular processes and inhibiting cell division in cancer cells. Additionally, nanoclays can adsorb biomolecules, including proteins, onto their surfaces. This can alter the cellular microenvironment and affect the signalling pathways that cancer cells rely on for growth and survival. Moreover, nanoclays can release ions such as magnesium or iron, when exposed to the intracellular environment of cancer cells. These ions can disrupt cellular processes and inhibit cancer cell growth. Nanoclays can also generate reactive oxygen species (ROS) when exposed to cellular environments. Elevated ROS levels can lead to oxidative stress in cancers cells, causing damage to cellular components and ultimately inhibiting cell proliferation. However, it is important to note that nanoclays are generally considered biocompatible and do not inherently harm or damage living cells. Findings from *in vitro* studies may not fully represent the complexity of interaction that occurs in living cells, therefore, it's essential to conduct *in vivo* studies in animal models to assess the overall toxicity and safety of nanoclays in a more physiological context. The use of a phenoxyaniline-based macroinitiator for producing these composites is a novel approach. Adding different weight percentages of Cloisite 93A to the polymer matrixes facilitates enhancement of its biochemical properties and crucial applications, where the biocompatibility and bioactivity are essential, such as in medical or pharmaceutical formulations. The excellent anticancer properties, including cancer cell apoptosis induction, hold significant importance in medicine and oncology. Furthermore, utilizing nanoclays for cancer treatment owing to their complete water solubility and ability to form cationic complexes with drugs through electrostatic interactions is an innovative approach. Experimental conditions are carefully controlled to ensure accurate and reproducible results, including temperature, pressure, reactant concentration and specific equipment for characterization and analysis process. Introducing the impact of nanoclay on phenoxy-based PMMA composites for anticancer treatment could be a new and pioneering development in the field. Further, we also confirmed their structural identifications by FT-IR, Raman, UV-vis and XRD. Interestingly, layer by layer crystals were formed and confirmed by SEM. In conclusion, to the best of our knowledge, this is the first time to employ such kind of block polymer nanocomposite through SET-LRP for cancer treatment against PC-3 and A-549 cell lines.

4 Conclusions

We have successfully synthesized phenoxyaniline-*b*-PMMA *via* controlled radical polymerization (SET-LRP) using a phenoxyaniline based macroinitiator and characterized it by various analytical techniques. Here, we showed that there were differential cellular responses in both prostate and lung cancer cell lines. Polymer containing cationic nanoclay was favoured to inhibit the cancer cell proliferation through electrostatic interaction. It showed an excellent cytotoxic effect in both cancer cell lines by using MTT assay and their bright green nucleus (viable cells), bright orange nucleus (early apoptotic cells – fragmented chromatin nucleus) and bright red nucleus (late apoptotic cells) were successfully identified by fluorescence microscopy. The number of cells was decreased after treatment and the cells exhibited cell shrinkage and cytoplasmic membrane blebbing. As a result, our study suggested that the prepared polymeric nanocomposites could be effective alternative materials in precision anti-cancer medicine. The analysis of the dynamics of individual interactions within cells is in progress.

Author contributions

Writing – original draft preparation, conceptualization and methodology: S. P., A. M., and S. M.; formal analysis: A. L., S. S., and D. M.; funding, review and editing: R. R., S. S. H. and A. M. All authors have read and agreed to the published version of the manuscript.

Conflicts of interest

There are no conflicts to declare.

Acknowledgements

This research was supported by the National Research Foundation of Korea (NRF) (Grant No. 2020R1A6A1A03044512) and Korea Institute of Planning and Evaluation for Technology in Food, Agriculture and Forestry (IPET) funded by the Ministry of Agriculture, Food and Rural Affairs (MAFRA) (321027-5). The author (Dr A. Murali) is thankful to the Department of Science and Technology (DST), Govt. of India, grant no. DST/INSPIRE/04/2018/001762, for the DST Inspire Faculty Award.

References

1 J. Kim, Y. M. Lee, Y. Kang and W. J. Kim, Tumor-homing, size-tunable clustered nanoparticles for anticancer therapeutics, *ACS Nano*, 2014, **8**, 9358–9367.

2 Y. B. Liu, X. Gao, D. Deeb, C. Brigolin, Y. Zhang, J. Shaw, K. Pindolia and S. C. Gautam, Ubiqui-tin-proteasomal degradation of antiapoptotic survivin facilitates induction of apoptosis in prostate cancer cells by pristimerin, *Int. J. Oncol.*, 2014, **45**, 1735–1741.

3 Y. Kumar, N. K. Singh, V. D. I. Singh, I. Ali, R. K. Tiwari, A. Kumar and D. S. Pandey, DNA/Protein binding and anticancer activity of Zn (II) complexes based on azo-Schiff base ligands, *Inorg. Chim. Acta*, 2022, **538**, 120963.

4 F. Hosseini, F. Hosseini, S. M. Jafari and A. Taheri, Bentonite nanoclay-based drug-delivery systems for treating melanoma, *Clay Miner.*, 2018, **53**, 53–63.

5 H. A. Patel, R. S. Somani, H. C. Bajaj and R. V. Jasra, Nanoclays for polymer nanocomposites, paints, inks, greases and cosmetics formulations, drug delivery vehicle and waste water treatment, *Bull. Mater. Sci.*, 2006, **29**, 133–145.

6 K. Sparnacci, M. Laus, L. Tondelli, L. Magnani and C. Bernardi, Core–shell microspheres by dispersion polymer-ization as drug delivery systems, *Macromol. Chem. Phys.*, 2002, **203**, 1364–1369.

7 H. P. Zobel, J. Kreuter, D. C. Werner, R. Noe, G. Kumel and A. Zimmer, Cationic Polyhexylcyanoacrylate Nanopar-ticles as Carriers for Antisense Oligonucleotides, *Drug Delivery*, 1997, **7**, 483–493.

8 K. S. V. K. Rao, I. Chung, K. M. Reddy and C. Sik Ha, PMMA-based microgels for controlled release of an anticancer drug, *J. Appl. Polym. Sci.*, 2009, **111**, 845–853.

9 C. Geyik, M. Ciftci, B. Demir, B. Guler, A. B. Ozkaya, Z. P. Gumus, F. B. Barlas, D. O. Demirkol, H. Coskunol, S. Timur and Y. Yagci, Controlled release of anticancer drug Paclitaxel usingnano-structured amphiphilic star-hyperbranched blockcopolymers, *Polym. Chem.*, 2015, **6**, 5470–5477.

10 A. P. Seyedeh, S. Saremi, S. N. Ostad, R. Dinarvand and F. Atyabi, Discriminated effects of thiolated chitosan-coated pMMA paclitaxel-loaded nanoparticles on different normal and cancer cell lines, *Nanomedicine*, 2010, **6**, 689–697.

11 M. F. Cury-Boaventura, C. Pompéia and R. Curi, Comparative toxicity of oleic acid and linoleic acid on Jurkat cells, *Clin. Nutr.*, 2004, **23**, 721–732.

12 J. i. Li, R. Hu, H. Zhou, S. Tao and Y. Wang, Nano-SiO2@PMMA-doped composite polymer PVDF-HFP/PMMA/PEO electrolyte for lithium metal batteries, *J. Mater. Sci.: Mater. Electron.*, 2020, **31**, 2708–2719.

13 C. M. Mathew, K. Kesavan and S. Rajendran, Structural and Electrochemical Analysis of PMMA Based Gel Elec-trolyte Membranes, *Int. J. Electrochem. Sci.*, 2015, 1–7.

14 G. Mingming, S. Aman and P. L. Robert, Impact of moderate pump–Stokes chirp on femtosecond coherent anti-Stokes Raman scattering spectra, *J. Raman Spectrosc.*, 2020, **51**, 115–124.

15 A. Arora, V. Choudhary and D. K. Sharma, Effect of clay content and clay/surfactant on the mechanical, thermal and barrier properties of polystyrene/organoclay nanocomposites, *J. Polym. Res.*, 2011, **18**, 843–857.

16 A. Elhussein, I. Tynga, M. A. El-Harith and H. Abrahamse, Photodynamic ability of silver nanoparticles in induc-ing cytotoxic effects in breast and lung cancer cell lines, *Int. J. Nanomed.*, 2014, **9**, 3771–3780.

17 S. L. Manoto and H. Abrahamse, Effect of a newly synthesized Zn sulfophthalocyanine derivative on cell morphol-ogy, viability, proliferation, and cytotoxicity in a human lung cancer cell line (A549), *Lasers Med. Sci.*, 2011, **26**, 523–530.

18 D. Ezhilarasan and V. S. Apoorva, Syzygium cumini extract induced reactive oxygen species-mediated apoptosis in human oral squamous carcinoma cells, *J. Oral Pathol. Med.*, 2019, **48**, 115–121.

19 S. Usmani, A. Hussain, A. H. A. Farooqui, M. Arshad, S. Siddiqui, M. Ahmad and S. Wahab, Anti-proliferative Activity of Crude Extract and Fractions Obtained from Digera muricata on HeLa Cell Lines of Human Cervix and A549 Cell Lines of Human Lung, *Pharmacogn. J.*, 2014, **6**, 32–38.

20 P. Suresh, K. Marimuthu, S. Ranganathan and T. Rajmohan, Optimization of machining parameters in turning of Al-SiC-Gr hybrid metal matrix composites using grey-fuzzy algorithm, *Trans. Nonferrous Met. Soc. China*, 2014, **24**, 2805–2814.

21 A. Sathivel, H. R. B. Raghavendran, P. Srinivasan and T. Devaki, Anti-peroxidative and anti-hyperlipidemic nature of Ulva lactuca crude polysaccharide on D-galactosamine

induced hepatitis in rats, *Food Chem. Toxicol.*, 2008, **46**, 3262–3267.

22 L. Govindaraju, P. Neelakantan and J. L. Gutmann, Effect of root canal irrigating solutions on the compressive strength of tricalcium silicate cements, *Clin. Oral Investig.*, 2017, 567–571.

23 T. Sathish and S. Karthick, Wear behaviour analysis on aluminium alloy 7050 with reinforced SiC through taguchi approach, *J. Mater. Res. Technol.*, 2020, **9**, 3481–3487.

24 H. Krishnaswamy, S. Muthukrishnan, S. Thanikodi, G. Arockiaraj and V. Venkatraman, Investigation of air conditioning temperature variation by modifying the structure of passenger car using computational fluid dynamics, *Therm. Sci.*, 2020, 495–498.